

12854

ROTORDYNAMIC FORCES IN LABYRINTH SEALS: THEORY AND EXPERIMENT

p. 29

Knox T. Millsaps* and Manuel Martinez-Sanchez
Massachusetts Institute of Technology
Cambridge, Massachusetts

ABSTRACT

A theoretical and experimental investigation of the aerodynamic forces generated by a single gland labyrinth seal executing a simultaneous spinning/whirling motion has been conducted. A lumped parameter model for a single gland seal with coupling to an upstream cavity with leakage is developed along with an appropriate solution technique. From this theory, it is shown that the presence of the upstream cavity can, in some cases, augment the cross-stiffness and direct damping by a factor of four. The parameters that govern the coupling are presented along with predictions on their influence. A simple uncoupled model is used to identify the mechanisms responsible for cross force generation. This reduced system is nondimensionalized and the physical significance of the reduced parameters is discussed. Closed form algebraic formulas are given for some simple limiting cases. It is also shown that the total cross-force predicted by the uncoupled model can be represented as the sum of an ideal component due to an inviscid flow with entry swirl and a viscous part due to the change in swirl created by friction inside the gland. The frequency dependent ideal part is solely responsible for the rotordynamic direct damping. The facility designed and built to measure these frequency dependent forces is described. Experimental data confirm the validity and usefulness of this ideal/viscous decomposition. A method for calculating the damping coefficients based on the force decomposition using only the static measurements is presented. Experimental results supporting the predicted cross force augmentation due to the effect of upstream coupling are presented.

* Present address: Naval Postgraduate School, Monterey, CA 93943.

NOMENCLATURE

<u>Symbol</u>	<u>Definition (units, SI)</u>
C_{xx}	Direct damping. (N s/m)
C_{xy}	Cross damping. (N s/m)
$C_{xx}^{**} = \frac{C_{xx}\delta_1^*}{IR_s^2\sqrt{P_i - P_o}}$	Non-dimensional direct damping. [1]
$C_{xy}^{**} = \frac{C_{xy}\delta_1^*}{IR_s^2\sqrt{P_i - P_o}}$	Non-dimensional cross damping. [1]
$D = \delta_1^* / h$	Nondimensional sealing gap. [1]
F_N	Force acting on the rotor in the direction of instantaneous displacement. (N)
F_T	Force acting on rotor in the direction tangent to the instantaneous displacement.(N)
F_R	Frictional(viscous) cross force component.(N)
F_G	Ideal cross force component. (N)
$H = h / R_s$	Nondimensional depth of labyrinth knife. [1]
h	Depth of seal gland. (m)
h_i	Depth of cavity upstream of seal. (m)
$i = \sqrt{-1}$	
$K = \kappa / \mu_2^*$	Normalized energy carry-over factor.[1]
K_{xx}	Direct stiffness. (N/m)
K_{xy}	Cross stiffness. (N/m)
$K_{xx}^{**} = \frac{K_{xx}\delta_1^*}{IR_s(P_i - P_o)}$	Nondimensional direct stiffness. [1]
$K_{xy}^{**} = \frac{K_{xy}\delta_1^*}{IR_s(P_i - P_o)}$	Nondimensional cross stiffness. [1]
$L = 1 / R_s$	Nondimensional labyrinth sealing pitch. [1]
l	Sealing pitch. (m)
l_i	Axial gap from the vanes to seal inlet. (m)
$P = P^*(1 + \xi)$	Static pressure in the labyrinth gland.(Pa)
P_i	Total pressure upstream of first knife. (Pa)
P_o	Static pressure downstream of seal. (Pa)
q_1	Flow rate through first knife/length(kg/m s)
q_2	Flow rate through second knife. (kg/m s)
R_s	Gas constant for air. 287.15 (J/ kg K)
r	Radial displacement of whirling shaft. (m)
\hat{r}	Magnitude of radial displacement. (m)
$S = \frac{\omega R_s}{V^*}$	Nondimensional spin rate. [1]
T	Air temperature. (K)
t	Time. (s)
$V = V^*(1 + \eta)$	Swirl velocity inside the seal gland. (m/s)
$W = \frac{\Omega R_s}{V^*}$	Nondimensional whirling frequency. [1]

$\alpha = \delta_2^* / \delta_1^*$	Nondimensional divergence. [1]
$\beta = \mu_2 / \mu_1$	Kinetic energy carry-over coefficient. [1]
$\Gamma = 1 - \frac{V_1}{V_2}$	Nondimensional swirl gradient parameter. [1]
$\Delta = \frac{q^*}{\mu_1^* \delta_1^* \rho^* \sqrt{R_s T}}$	Nondimensional seal flow rate. [1]
δ_1, δ_2	Sealing gaps for the sealing knives. (m)
$\epsilon = r / \delta_1^*$	Nondimensional whirling eccentricity. [1]
λ_r	Darcy friction factor for the stator. [1]
λ_s	Darcy friction factor for the rotor. [1]
$\kappa = -C_c \frac{\partial \beta}{\partial r} \Big _{r=0}$	Kinetic energy carry-over sensitivity. (1/m)
μ_1, μ_2	Flow coefficients for the sealing knives. [1]
$\xi = \hat{\xi} e^{i(\theta - \Omega t)}$	Harmonic pressure perturbation. [1]
$\eta = \hat{\eta} e^{i(\theta - \Omega t)}$	Harmonic velocity perturbation. [1]
ρ	Fluid density. (kg/m ³)
$\sigma = \frac{\rho^* \delta_1^* V^*}{q^*}$	Nondimensional swirl parameter. [1]
$\bar{\sigma} = \sigma(1 - W)$	Swirl parameter as observed in whirling reference frame. [1]
Ω	Whirling frequency of the shaft. (1/s)
ω	Shaft rotational speed. (1/s)
$[\]^*$	Steady solution for the case of centered rotor.
$[\]_1, [\]_2$	Quantities at the first or second knife respectively.

1. INTRODUCTION

One of the major sources of rotordynamic instabilities in high power-density turbomachinery is asymmetric pressure distributions in the glands of labyrinth seals which generate cross forces. If the net seal force tangent to the instantaneous whirling displacement is in the direction of this whirl, instability will be promoted. The possibility of labyrinth seals creating unstable rotor whirl has been known since the 1940's as reported by Den Hartog [1]. Alford [2] and Thomas [3] were the first to propose analytical models for the prediction of labyrinth seal forces. However, neither of these models is particularly useful, because the influence of the inlet swirl, which is known to dominate in the generation of cross forces, was neglected by both authors. A lumped parameter model that couples the axial flow over the knives to one-dimensional continuity and momentum equations inside the seal gland was developed by Kostyuk [4]. The gland-depth variation with rotor eccentricity was neglected and hence no cross stiffness nor direct damping is predicted from this model for a rotor whirling with a parallel precession. Subsequently, Iwatsubo [5] added the necessary term to account for this variation. Many other authors, including Gans [6], Kurahasi and Inoue [7], Fujikawa, Kameoka and Abe [8], Scharrer and Childs [9], and Martincz and Lee [10], have used similar lumped parameter models to predict the cross forces for a great variety

of geometries and flow conditions. All of these models have assumed constant upstream and downstream boundary conditions.

Analyses that consider variations within each seal gland, by using multi-control volumes within each seal gland, have been conducted [8,11]. However, this approach is cumbersome and the different control volumes must be coupled with ad-hoc assumptions or analysis. No advantages have been clearly shown from such models over the single control volume models.

Computational Fluid Dynamics (CFD) methods have also been used, most notably by Nordmann and Weiser [12], to predict results similar to those obtained by the lumped parameter models. These codes may be very useful in modeling some of the detailed flow fields in the glands, which can be used for the sub-models to predict carry-over coefficient variation, friction factors, etc. However, it appears that the simple lumped parameter models contain the dominant fluid physics, which is asymmetric injection of swirl momentum, necessary to predict destabilizing forces, at least for multi-cavity seals.

All of these analyses have assumed uniform upstream and downstream boundary conditions. These assumptions may not be adequate for the prediction of the rotordynamic forces in short seals, where the end conditions may greatly affect the perturbations in both pressure and the swirl component of velocity.

The first experiments to measure the self-exciting forces in isolated labyrinths were those of Benckert and Wachter [13,14,15], who measured the static pressure distributions around the casing and integrated them to find the direct and cross forces due to a statically offset rotor. Many different geometries were tested over a wide range of flow conditions. They determined the general pressure/inlet kinetic energy scaling parameters for statically offset seals. Brown and Leong [16], Thieleke and Stetter [17], Kanki and Morii [18] and Hisa, Sakakida and Asatu [19], have all made similar measurements yielding a good data base on the displacement dependent rotordynamic coefficients. Experimental investigations on the dynamic characteristics of labyrinths have been conducted by Wright [20], Kanemitsu and Ohsawa [21], Scharrer [22], Scharrer and Childs [23] and Millsaps and Martinez [24].

Kostyuk-type lumped parameter models are capable of predicting the cross-stiffness coefficients for long labyrinth seals (more than 6 chambers) to within 25% of the experimentally obtained values [10]. However, the situation with respect to short seals, and with the dynamic coefficients, especially the direct damping, has been far less satisfactory. The measured cross-stiffness coefficients in two and three gland seals, as measured by Benckert [12], are more than 100% larger than those predicted by theory in most cases. Measured dynamic coefficients for both long and short seals are not well predicted by theory. Discrepancies between the measured and predicted direct damping of nearly 500% are shown by Scharrer [21] for some conditions. While the results from many computations have been reported using the various lumped parameter models, little physical understanding on the mechanisms that generate dynamic forces has been obtained from the models. In particular, no analysis has been presented that clearly delineates the importance of the various geometric and flow related parameters and explains, in physical terms, the origin of the damping forces. The general mechanisms that

generate the static and dynamic force components in a spinning/whirling seal has not been adequately explained.

The purpose of this paper is to introduce a new analytical model which includes the effect of upstream coupling, which is believed to be responsible for the much higher than expected cross stiffness and direct damping obtained experimentally, and to describe the nature and mechanisms of the damping forces in labyrinth seals.

In Section 2, an analytical model is presented that allows for non-uniform flow in the volume upstream of the whirling seal. Coupled continuity and momentum equations are given for both the whirling, single gland seal with the added terms due to the non-uniform inlet, and for the non-whirling, finite volume upstream cavity which has a leakage path to a large center cavity. The addition of the extra leakage flow significantly complicates the solution of this system because it introduces an essential non-linearity. An approximate solution method is presented, based on harmonic averaging, to deal with this difficulty. The parameters that control the augmentation in cross forces are identified. Results from this new model are presented that show a large impact due to the non-uniform upstream flow field due to the coupling with the seal perturbations.

In Section 3 the general nature of cross forces in labyrinth seals is discussed. The mechanisms for the generation of rotordynamic damping will be delineated. All the physical arguments will be developed with uniform inlet conditions to avoid unnecessary algebraic complexity. However, all of the arguments to be presented can be readily generalized to account for the upstream non-uniformities. These reduced equations are nondimensionalized, and formulas for the frequency-dependent direct and cross forces are given. The physical significance of the various parameters is discussed, and the scaling behavior provided. The rotordynamically destabilizing cross force will be shown to be the sum of two distinct components. An "ideal" one due to an inviscid flow, and a "viscous" part due to frictional shear. The damping will be shown to originate entirely from the ideal component. From this decomposition, a method for extracting the damping coefficients from purely static measurements are shown.

In Section 4, the experimental apparatus and measurement methods used to determine these dynamic forces are described. The instrumentation and data analysis procedures are given.

In Section 5, comparisons of the theory to the experimental data will be provided. Although no precise comparison of the coupled model to the experimental data is possible due to the lack of control or measurement of the axial gap of the face seal which vents the upstream pressure perturbations to the center hub plenum. The experimental data support the use of the ideal/viscous decomposition for the determination of direct damping coefficients from purely static stiffness data. Also the theory is compared to the experimental results of Benckert for statically offset two and three chamber seals.

2. MODEL FOR UPSTREAM COUPLING

The experimental and analytical research proceeded initially on the assumption that the boundary conditions for the single gland labyrinth seal were uniform. That is, the whirling eccentric seal is fed by an upstream reservoir where the pressure and tangential velocity is

spatially and temporally uniform, and discharges to a downstream volume at a constant static pressure.

Indications that substantial upstream non-uniformity may exist and be of importance were provided from time resolved pressure measurements in the MIT Labyrinth Seal Test Facility (LSTF) with a whirling seal, just upstream of the first knife, and from steady pressure measurements in the MIT Alford Force Test Facility (AFTF) upstream and downstream of a statically off-set seal, that was attached to a shrouded turbine rotor.

The experimental values of cross stiffness and direct damping measured in the LSTF were consistently 2 to 4 times the values predicted by the lumped parameter model. Several attempts were made to reconcile the simple model with the experiments by parameterically varying the sub-model coefficients such as friction factors, discharge coefficients, kinetic energy carry-over coefficients, etc. It was found that, within reasonable ranges of variation, no combination of these coefficients would yield results in agreement with the experimental data. Therefore, the basic assumptions of the model were investigated. This reassessment led to an extended model where variations in the upstream flow, induced by the flow perturbations in the gland itself are included. This extended theory is capable of predicting the high force levels that were measured.

Before embarking upon algebraic manipulations, it is useful to provide a qualitative description of the coupling mechanisms involved. When the shaft is offset and the sealing gap varies around the seal perimeter, a low pressure area will develop upstream of the seal in the vicinity of the widest gap. Because of this, the velocity magnitude will be higher there, and, in particular, the all-important tangential velocity will have a relative maximum near the widest gap. When the fluid carrying this excess tangential momentum enters the seal cavity and mixes with the swirling seal flow, it will preferentially energize it in this area. The result will be a positive pressure gradient, $(\partial P / \partial \theta)$, in this area, and hence a maximum P in the seal about 90° ahead of this maximum gap. This will then produce a forward whirling force. For a concrete formulation of these effects, consider the geometry of Figure 1. This geometry reflects that of the LSTF and most other test section configurations that have been used to measure rotordynamic forces. The swirl vanes, which are located l_i upstream from the first knife, have an effective radial gap of δ_v . There is some reduction of the effective flow area due the vane metal and boundary layer blockage. These vanes deliver air into the first cavity with an effective swirl angle of α_v , which is the metal angle minus some small turning deviation. The cavity is h_i deep and is sealed from a large center volume by an axial face labyrinth seal with a gap of δ_c . Since there is no net flow into this center cavity, the pressure here is uniform and the same as in the swirl cavity, namely P_i^* . The one-dimensional continuity equation for the upstream cavity (swirl chamber) is

$$\frac{\partial}{\partial t}(\rho_i l_i h_i) + \frac{1}{R_i} \frac{\partial}{\partial \theta}(\rho_i l_i h_i V_i) + q_i - q_v + q_{c,out} - q_{c,in} = 0 \quad (1)$$

where V_i is no longer constant, q_v is the flow rate per unit length issuing from the swirl vanes and the q_c 's are the radial flows in and out of the center cavity, respectively. Incompressible relations are sufficient for treating these flows since the transfer velocities are very low. These flows can be written as

$$q_c = \mu_c \delta_c \sqrt{2\rho_i^* (P_i - P_i^*)} \quad (2)$$

This relation is fundamentally different from those for q_v , q_1 and q_2 in that there is no flow to or from the center volume when the seal is centered in the casing because $P_i = P_i^*$. This introduces an essential nonlinearity into the analysis and hence must be dealt with in a different manner. Likewise the momentum equation in this cavity is

$$\begin{aligned} \frac{\partial}{\partial t}(\rho_i l_i h_i V_i) + \frac{1}{R_s} \frac{\partial}{\partial \theta}(\rho_i l_i h_i V_i^2) + q_1 V_i - q_v V_v \\ + q_{c,out} V_i - q_{c,in} V_c + \tau_s(2l_i + h_i) - \tau_r h_i + \frac{l_i h_i}{R_s} \frac{\partial P_i}{\partial \theta} = 0 \end{aligned} \quad (3)$$

where V_c is the swirl velocity inside the center volume. In this cavity the cross sectional area, $l_i h_i$, and the vane gap, δ_v^* , are constant. However, the inlet swirl component of velocity, V_v , is not. The angle of the fluid leaving the vanes, α_v , is constant. Therefore, a drop in the pressure at one location in this cavity will induce a greater mass influx and hence a higher swirl velocity at that location. This is the essence of the mechanism that augments the forces.

The usual 1-D continuity and momentum equations for the seal gland as presented by many Authors [5,6,8,9,10] are still valid within the constraints of the model, except that their linearization will yield additional terms from the upstream pressure and velocity non-uniformities. The continuity equation is

$$\frac{\partial[\rho l(h + \delta_1)]}{\partial t} + \frac{1}{R_s} \frac{\partial}{\partial \theta}[\rho l(h + \delta_1)V] + q_2 - q_1 = 0 \quad (4)$$

and the momentum equation is

$$\frac{\partial[\rho l(h + \delta_1)V]}{\partial t} + \frac{1}{R_s} \frac{\partial}{\partial \theta}[\rho l(h + \delta_1)V^2] + q_2 V - q_1 V_i + \tau_s l - \tau_r(l + 2h) + \frac{lh}{R_s} \frac{\partial P}{\partial \theta} = 0 \quad (5)$$

and the q 's, other than those to and from the center cavity, are given by

$$q_1 = \frac{\mu_1 \delta_1}{\sqrt{R_s T}} (P_i^2 - P^2)^{\frac{1}{2}} \quad q_2 = \frac{\mu_2 \delta_2}{\sqrt{R_s T}} (P^2 - P_o^2)^{\frac{1}{2}} \quad q_v = \frac{\mu_v \delta_v}{\sqrt{R_s T}} (P_\infty^2 - P_i^2)^{\frac{1}{2}} \quad (6)$$

The same linear perturbation solution procedure used for the single gland seal with no upstream coupling can be used when there is no flow into the center cavity. However, as previously stated the nature

of the oscillating flow between the two upstream volumes requires some modifications and careful treatment. This is because these oscillating leakage flows vary as $\sqrt{\bar{P}_i}$, where \bar{P}_i is the upstream pressure perturbation, rather than linearly with \bar{P}_i (first order) or P_i (zeroth order) like the others. Thus, their effect can be disproportionately great at small offset amplitudes.

First the zeroth order solutions are obtained for the centered rotor. The velocity, pressure and density in the upstream swirl cavity will be denoted by V_i^* , P_i^* and ρ_i^* respectively and similarly in the seal gland, V^* , P^* and ρ^* . The pressure and velocity in the swirl cavity are expressed as

$$P_i = P_i^* (1 + \hat{\xi}_i e^{i(\theta - \Omega t)}) \quad V_i = V_i^* (1 + \hat{\eta}_i e^{i(\theta - \Omega t)}) \quad (7)$$

and in the seal gland by

$$P = P^* (1 + \hat{\xi} e^{i(\theta - \Omega t)}) \quad V = V^* (1 + \hat{\eta} e^{i(\theta - \Omega t)}) \quad (8)$$

Where it is understood that the real part of all expressions are to be used. The perturbation expressions for $\hat{\xi}_i$, $\hat{\eta}_i$, $\hat{\xi}$ and $\hat{\eta}$ are substituted into the continuity and momentum equations for both the upstream swirl cavity and the seal gland. The nondimensional perturbation leakage flow into the center cavity is

$$\frac{q_c}{q^*} = \frac{\mu_c \delta_c}{\mu_1 \delta_1} \sqrt{\frac{2P_i^*}{P_i^* - P^*}} \left[\text{Re} \left\{ \hat{\xi}_i e^{i(\theta - \Omega t)} \right\} \right]^{\frac{1}{2}} \quad (9)$$

The first harmonic component of this function will be extracted by averaging over one period. The first harmonic of the perturbation reduces, after some manipulation, to

$$\left[\text{Re} \left\{ \hat{\xi}_i e^{i\psi} \right\} \right]^{\frac{1}{2}} = \frac{4\sqrt{|\hat{\xi}_i|}}{\pi} \int_0^{\frac{\pi}{2}} \cos^{\frac{3}{2}} \Psi d\Psi = \frac{4\sqrt{|\hat{\xi}_i|}}{\pi} \sqrt{2} \cdot B\left(\frac{5}{4}, \frac{5}{4}\right) \quad (10)$$

Where B is the beta function. From this the first harmonic of $q_{c,out} - q_{c,in}$ is found to be

$$\frac{\bar{q}_c}{q^*} = 1.57377 \frac{\mu_c \delta_c}{\mu_1 \delta_1} \sqrt{\frac{P_i^*}{P_i^* - P^*}} |\hat{\xi}_i|^{-1/2} \hat{\xi}_i e^{i(\theta - \Omega t)} \quad (11)$$

Similarly the first harmonic of $q_{c,out} V_1 - q_{c,in} V_c$ is

$$1.57377 \frac{\mu_c \delta_c}{\mu_1 \delta_1} \sqrt{\frac{2P_i^*}{P_i^* - P^*}} |\hat{\xi}_i|^{-1/2} \frac{1}{2} (V_c^* + V_i^*) \hat{\xi}_i e^{i(\theta - \Omega t)} \quad (12)$$

The first harmonic of the perturbation continuity equation for the swirl cavity, after dividing by q^* is

$$\left\{ \frac{1.57377\mu_c^*\delta_c}{\mu_i^*\delta_i^*\sqrt{|\hat{\xi}_i|}} \left[\frac{P_i^{*2}}{P_i^{*2} - P^{*2}} \right]^{\frac{1}{2}} + \left[\frac{P_i^{*2}}{P_\infty^{*2} - P_i^{*2}} + \frac{P_i^{*2}}{P_i^{*2} - P^{*2}} \right] + \right\} \left\{ \frac{\rho_i^* l_i h_i}{\gamma_i^*} \left(\frac{V_i^*}{R_s} - \Omega \right) i \right\} \hat{\xi}_i + \left\{ \frac{\rho_i^* V_i^* l_i h_i}{R_s q^*} i \right\} \hat{\eta}_i - \left\{ \frac{P^{*2}}{P_i^{*2} - P^{*2}} \right\} \hat{\xi}_i = \left\{ \frac{1}{\delta_i^*} \right\} \hat{r} \quad (13)$$

and the swirl cavity momentum equation after dividing by $q^* V_i^*$ is

$$\left\{ \frac{0.78688\mu_c^*\delta_c \left(1 + \frac{V_c^*}{V_i^*} \right)}{\mu_i^*\delta_i^*\sqrt{|\hat{\xi}_i|}} \left[\frac{P_i^{*2}}{P_i^{*2} - P^{*2}} \right]^{\frac{1}{2}} + \left[\frac{P_i^{*2}}{P_i^{*2} - P^{*2}} \right] + \right\} \left(\frac{V_y}{V_i^*} \right) \left(\frac{P_i^{*2} + P_\infty P_i^*}{P_\infty^2 - P_i^{*2}} \right) + \frac{\lambda_{si} \rho_i^* (l_i + h_i) V_i^*}{4\gamma_i^*} + \left\{ \left[\frac{\rho_i^* l_i h_i}{\gamma_i^*} \left(\frac{V_i^*}{R_s} - \Omega \right) + \frac{P_i^* l_i h_i}{V_i^* q^* R_s} \right] i \right\} \hat{\xi}_i + \left\{ 1 + \frac{\lambda_{si} \rho_i^* (l_i + h_i) V_i^*}{2\gamma} + \left[\rho_i^* l_i h_i \left(\frac{2V_i^*}{R_s} - \Omega \right) \right] i \right\} \hat{\eta}_i + \left\{ \frac{P^{*2}}{P_i^{*2} - P^{*2}} \right\} \hat{\xi}_i = \left\{ \frac{1}{\delta_i^*} \right\} \hat{r} \quad (14)$$

The nondimensional continuity equation for the seal gland, which includes the effect of the upstream cavity coupling is

$$\left\{ \frac{-P_i^{*2}}{P_i^{*2} - P^{*2}} \right\} \hat{\xi}_i + \left\{ \left[\frac{P^{*2}}{P^{*2} - P_o^2} + \frac{P^{*2}}{P_i^{*2} - P^{*2}} \right] + \frac{\rho^* l h}{\gamma_i^*} \left(\frac{V^*}{R_s} - \Omega \right) i \right\} \hat{\xi}_i + \left\{ \frac{\rho^* V^* l h}{R_s q^*} i \right\} \hat{\eta}_i = \left\{ \frac{\kappa}{\mu_2^*} + \left(\frac{1}{\delta_2^*} - \frac{1}{\delta_1^*} \right) + \frac{\rho^* l}{q^*} \left(\frac{V^*}{R_s} - \Omega \right) i \right\} \hat{r} \quad (15)$$

and the coupled momentum equation for the seal gland is

$$\left\{ \left(\frac{V_i^*}{V^*} \right) \frac{-P_i^{*2}}{P_i^{*2} - P^{*2}} \right\} \hat{\xi}_i + \left\{ \frac{-V_i^*}{V^*} \right\} \hat{\eta}_i + \left\{ \frac{P^{*2}}{P^{*2} - P_o^2} + \left(\frac{V_i^*}{V^*} \right) \frac{P^{*2}}{P_i^{*2} - P^{*2}} + \left(\frac{\rho^*}{8\gamma_i^* V^*} \right) (\lambda_{si} l V^{*2}) \right\} \left\{ -\lambda_r (1 + 2h) (\omega R_s - V^*)^2 + \left[\frac{\rho^* l h}{\gamma_i^*} \left(\frac{V^*}{R_s} - \Omega \right) + \frac{\rho^* l h R_s T}{R_s} \right] i \right\} \hat{\xi}_i + \left\{ 1 + \frac{\rho^*}{4q^*} (\lambda_{si} l - \lambda_r (1 + 2h) (V^* - \omega R_s)^2) + \rho^* l h \left(\frac{2V^*}{R_s} - \Omega \right) i \right\} \hat{\eta}_i = \left\{ \frac{\kappa}{\mu_2^*} + \frac{1}{\delta_2^*} - \frac{V_i^*}{V^* \delta_1^*} + \frac{\rho^* l}{q^*} \left(\frac{V^*}{R_s} - \Omega \right) i \right\} \hat{r} \quad (16)$$

This can be written compactly in matrix form as

$$\begin{pmatrix} Z_{1,1} & Z_{1,2} & Z_{1,3} & Z_{1,4} \\ Z_{2,1} & Z_{2,2} & Z_{2,3} & Z_{2,4} \\ Z_{3,1} & Z_{3,2} & Z_{3,3} & Z_{3,4} \\ Z_{4,1} & Z_{4,2} & Z_{4,3} & Z_{4,4} \end{pmatrix} \begin{pmatrix} \hat{\xi}_i \\ \hat{\eta}_i \\ \hat{\xi}_s \\ \hat{\eta}_i \end{pmatrix} = \begin{pmatrix} R_1 \\ R_2 \\ R_3 \\ R_4 \end{pmatrix} \hat{r} \quad (17)$$

This is not a linear system. The elements $Z_{1,1}$ and $Z_{2,1}$ contain $|\hat{\xi}_i|^{-1/2}$. Of course if $\hat{\xi}_i = \hat{\eta}_i = 0$ the system decouples and the original 2x2 system for the isolated seal with no upstream coupling is recovered. To solve this system a simple iteration scheme was employed. Equation (17) is first solved with $\delta_c = 0$ then from this solution, $\hat{\xi}_i^1$, is used on the left hand side to calculate an updated solution. This iteration procedure continues until a predetermined convergence criterion is satisfied

$$|\hat{\xi}_i^{n+1} - \hat{\xi}_i^n| < \epsilon \quad (18)$$

Now this model shall be used for predicting the influence of this coupling mechanism. In addition to the parameters that control the generation of rotordynamic forces for an isolated seal, the parameters that characterize the influence of the upstream coupling are

1. The ratio of the swirl cavity area to the seal gland area, $(l_i h_i)/(lh)$.
2. The relative size of the axial sealing gap compared to the radial gap, δ_c / δ_1^* .
3. The swirl velocity inside the center cavity, V_c . This is strongly influenced by rotation of the seal disk.
4. The relative whirl eccentricity, \hat{r} / δ_1^* . This is a purely non-linear effect. For the linear system all of the forces are directly proportional to the whirl eccentricity.

The effects of the cross force augmentation of each parameter will now be considered separately. According to the model, if there is no leakage into the center cavity, the effect of the upstream coupling always acts to increase the magnitude of both the cross stiffness and direct damping, and in the same proportions. Figure 2 shows the ratio of the direct damping from the coupled model, with $\delta_c = 0$, to that of the uncoupled one for various swirl chamber to seal area ratios. As the swirl cavity area approaches zero the predicted force augmentation does not vanish but, approaches a value of 1.62. This residual effect in the absence of the first cavity is due to the condition imposed at the swirl vanes. In the simple model V_i is constant. If instead the vanes are close coupled a reduction in the gland pressure will still bring in more flow and hence will induce a higher swirl component locally. The maximum increase in the cross stiffness and direct damping over the uncoupled model is about 4.42 and occurs at an area ratio, $(l_i h_i)/(lh)$ of 1.35. Even at

an area ratio of 10 the forces are increased by a factor of two. The force predicted by the coupled model asymptotically approaches the uncoupled one as $(l_i h_i)/(lh) \rightarrow \infty$. The coupled and uncoupled models match to within 1% for an area ratio of about 80. Well before this value the assumptions of the model probably break down. In particular, significant variations in the perturbation quantities are likely to occur in the axial direction within the swirl cavity.

The presence of the axial clearance between the swirl cavity and the large center volume permits for a "venting" that reduces the magnitude of $\hat{\xi}_i$. This effect tends to mitigate the large augmentation of the forces that the upstream cavity may induce. Figure 3 shows the direct and cross force vs. the relative leakage area δ_c/δ_1^* . It is assumed that $V_c = V_1^*$ for simplicity. As δ_c goes from 0 to ∞ both force components go from the fully coupled values to those predicted by the uncoupled model. However, this does not occur when $V_c \neq V_1^*$. The forces are very sensitive to small changes in the axial gap when it is less than δ_1^* . However, when $\delta_c/\delta_1^* > 1$, there is a greatly reduced sensitivity to small changes in axial gap.

The model predicts that the swirl velocity inside the center volume can have a minor impact, on the order of 10-20%, on the seal pressure perturbations. For cases where there is no seal rotation it is probably safe to assume that $V_c = 0$. This is because the tangential momentum feed into the seal is of perturbation order and the shear stresses acting to retard the flow are of order unity. For cases with seal rotation, it would be very difficult to estimate the swirl velocity inside the center cavity. Figure 4 shows the effect that changes in the center cavity swirl velocity have on the forces.

In the absence of the leakage flow non-linearity, the theory predicts that the forces should scale with whirl eccentricity and hence the rotordynamic coefficients, and should be independent of the whirl amplitude. The nonlinearity due to axial leakage is shown in Figure 5, which shows K_{xx} and K_{xy} the relative eccentricity \hat{r}/δ_1^* . The behavior of C_{xx} is the same as for K_{xy} . The direct force is much more sensitive to the whirl amplitude than is the cross force. At large whirl amplitudes, the predicted forces approach those obtained for $\delta_c = 0$ (i.e. the fully coupled case). However, as $r \rightarrow 0$ the center leakage flow is able to "kill" the swirl cavity pressure perturbation completely. This effectively decouples the whirling seal from the upstream cavity.

3. IDEAL - VISCOUS FORCE DECOMPOSITION

It will now be shown that within the constraints of the lumped parameter model, the total cross force can be separated into two additive components. One of these is the ideal part, due to an inviscid inlet flow with entry swirl, and the other is the viscous part, due to the change in swirl brought about by frictional shear stresses in the gland.

The following development shall be done without consideration of upstream coupling. However, all of the arguments can be readily generalized to account for such coupling.

In order to isolate these two contributions it is useful to nondimensionalize the continuity and momentum equations for the seal

gland. Equations (15) and (16) can be written in terms of the following non-dimensional parameters as

$$\left\{ \frac{1}{\Delta^2} + \left(\frac{\alpha \mu_2^*}{\Delta \mu_1^*} \right)^2 + \left[\frac{\sigma L}{\gamma D} (1-W) \right] i \right\} \hat{\xi} + \left\{ \frac{\sigma L}{D} i \right\} \hat{\eta} = \left\{ \left(\frac{1}{\alpha} - 1 \right) + K + \sigma L (1-W) i \right\} \hat{\epsilon} \quad (19)$$

and

$$\left\{ \frac{\sigma L}{8\gamma DH} \left(\lambda_s - \lambda_r \left(1 + \frac{2H}{L} \right) (S-1)^2 \right) - \frac{\Gamma}{\Delta^2} + \left[\frac{\sigma LW}{\gamma D} + \frac{L}{\Delta^2 \sigma \mu_1^{*2} D} \right] i \right\} \hat{\xi}$$

$$\left\{ 1 + \frac{\sigma L}{4DH} \left(\lambda_s - \lambda_r \left(1 + \frac{2H}{L} \right) (1-S) \right) + \frac{\sigma L}{D} (1-W) i \right\} \hat{\eta} = \Gamma \hat{\epsilon} \quad (20)$$

All of these non-dimensional parameters may be categorized as geometric, kinematic or flow related. The geometric ones are

$$\hat{\epsilon} = \frac{\hat{r}}{\delta_1^*} \quad \alpha = \frac{\delta_2^*}{\delta_1^*} \quad D = \frac{\delta_1^*}{h} \quad H = \frac{h}{R_s} \quad K = \frac{\delta_1^* \kappa}{\mu_2^*} \quad L = \frac{1}{R_s} \quad (21)$$

Note that K has been considered along with the geometric parameters because it is analogous to a convergent/divergent gap (Alford effect) in the effect that it has on the direct and cross forces. The kinematic parameters that specify the motion of the seal are

$$S = \frac{\omega R_s}{V^*} \quad W = \frac{\Omega R_s}{V^*} \quad (22)$$

and the dynamic parameters that indicate the axial flow rate or pressure gradient, the inlet swirl and the change in swirl respectively are

$$\Delta = \frac{q^*}{\mu_1^* \delta_1^* \rho^* \sqrt{R_s T}} \quad \sigma = \frac{\rho^* \delta_1^* V^*}{q^*} \quad \Gamma = 1 - \frac{V_i}{V^*} \quad (23)$$

There are two combinations of these parameters, $\sigma\Gamma$ and $\sigma(1-W)$, which will be shown to be very important.

Cramer's rule can be used to write an explicit expression for the nondimensional pressure perturbation which, upon integration, yields the forces acting on the rotor. The forces are proportional to $P^* \hat{\xi}$. In general the shear stresses may also contribute to the forces. However, from the equation solutions it has been shown that the shear forces due to velocity perturbations are small when compared to the forces arising from pressure perturbations [24]. For moderate whirl relative inlet swirl angles, which occurs providing the following condition is satisfied

$$\frac{1 + \alpha^2 \beta^2}{\Delta^2} \gg \frac{\sigma L}{\gamma D} (1-W) \quad (24)$$

the full expression may be simplified to yield the following real and imaginary parts for the pressure perturbation normalized by both the flow and eccentricity

$$\frac{\hat{\xi}_R}{\Delta^2 \varepsilon} = \frac{K - \left(1 - \frac{1}{\alpha}\right) - \frac{\sigma^2 L^2}{D} (1-W)^2}{1 + \alpha^2 \beta^2 + \frac{L^2}{D^2 \mu_1^2}} \quad (25)$$

$$\frac{\hat{\xi}_I}{\Delta^2 \varepsilon} = \frac{\frac{\sigma L}{D} \left[\Gamma + (1-W) \left(-D - K + 1 - \frac{1}{\alpha}\right) \right] i}{1 + \alpha^2 \beta^2 + \frac{L^2}{D^2 \mu_1^2}} \quad (26)$$

The first of these is real and therefore is in the direction of the minimum gap and hence is proportional to the direct force. The imaginary part is proportional to the destabilizing cross force. Both forces are proportional to $P^* \Delta^2$. For low inlet-to-exit pressure ratios, this reduces approximately to a simple pressure difference scaling, $P_i - P_o$, as one would expect for an incompressible flow. For this to hold, all of the other nondimensional parameters must be kept constant. In particular, the inlet swirl flow angle as observed from the whirling rotor must be fixed as the pressure difference is changed. As an example, if the axial pressure difference is increased the inlet swirl velocity and whirl speed must also be increased to maintain constant, σ and W , if this scaling is to be used. This is a generalization of the relationship used by Benckert [12] for statically offset seals.

The direct force is mainly due to the kinetic energy carry-over variations and differences in the nominal sealing clearances as seen in Equation (25). These effects generate a direct stiffness. The smaller terms, that are proportional to $\sigma^2 (1-W)^2$, generate direct inertia coefficients. It is possible that this direct force may alter the natural frequency of the rotor slightly. Therefore, no further discussion of the direct force will be given due to the small impact it has on rotordynamic stability.

The cross force can be seen from Equation (26) to be the summation of two terms, one proportional to $\sigma(1-W)$ and the other proportional to $\sigma\Gamma$. The nature of these two contributions and their crucial differences are very important and will lead directly to the cross force decomposition to be given. The kinetic energy carry-over term, K , and the "Alford" [2] term due to seal convergence/divergence, $(1-1/\alpha)$, do not generate cross force in the absence of swirl. But do alter this force in the presence of swirl. A convergent seal and/or kinetic energy carry-over will tend to increase the cross force magnitude. This is destabilizing when $W < 1$ or equivalently when the whirl frequency is less than V^*/R_s . However, this will enhance stability, in the forward direction, when Ω is greater than V^*/R_s .

The total cross force, F_T , will now be split into "ideal" and "viscous" contributions. The ideal or inviscid part, F_σ , is the cross force that would be generated in a purely inviscid fluid with inlet swirl. It is

proportional to $\sigma(1-W)$. The viscous contribution, F_r , which is proportional to $\sigma\Gamma$, is due to the frictional forces changing the swirl velocity inside the seal gland. The two forces tend to be of the same magnitude but, the nature of these two contributions is quite different. The ideal component is *dependent* on the rotor whirl frequency and hence will contribute to the direct damping. The viscous component is *independent* of the whirl speed and hence can not contribute to the direct damping. The frequency dependent behavior of a seal in an inviscid fluid can be readily explained by considering a simple change of reference frame. Let the relative inlet swirl, denoted by $\bar{V}_i = V_i - \Omega R_s$, be the inlet swirl velocity as measured by an observer rotating in the whirling frame. The non-dimensional swirl parameter in the whirling frame will be similarly denoted by $\bar{\sigma}$ and is

$$\bar{\sigma} = \sigma(1-W) = \frac{\rho^* \bar{V}_i^* \delta_i^*}{q^*} \quad (27)$$

The cross force generated by an inviscid flow at an inlet swirl of V_i at a frequency of Ω is identically the same as the cross force that would be generated for a static offset with the associated relative inlet swirl of \bar{V}_i . This equivalence can be seen by noting that the governing continuity and momentum equations are invariant under Galilean transformation. As a particular case of this argument, consider a rotor whirling so that the minimum gap is traveling at the same speed as the inlet swirl. Then there is no swirl relative to the rotating frame observer. Therefore the inviscid cross force must be zero when $\Omega = V_i/R_s$, or equivalently when $W=1$. This behavior is very similar to the quasi-static oscillation of an airfoil. The damping force there is related to the induced angle of attack due to the vertical motion. For the case of the whirling rotor, it is the "induced" inlet swirl angle change, due to the whirling motion, that creates the rotordynamic damping. Figure 6 shows the analogy between these two phenomena.

This simple behavior for both the airfoil and the rotor is limited to the quasi static case. For the rotor, this condition of low reduced frequency, is satisfied when the fluid residence time in the seal is short when compared to the period of oscillation of the rotor. This can be expressed as

$$\frac{\Omega l}{V_x} \ll 1 \quad (28)$$

where V_x is the axial velocity through the seal. An interesting and useful consequence of this relationship between the static and dynamic forces, is that in the absence of viscosity the direct damping, C_{xx} , can be calculated from purely static measurements of the cross stiffness, K_{xy} , versus the inlet swirl by

$$C_{xx} = R_s \frac{dK_{xy}(V_i)}{d(V_i)} \quad (29)$$

If the stiffness is a linear function of the inlet swirl, then a single measurement of the cross stiffness is needed to find the damping behavior.

$$C_{xx} = R_s \frac{K_{xy}(V_i)}{V_i} \quad (30)$$

A similar argument can be used to extract the direct damping coefficient from the static coefficient measurements in the presence of viscosity. However, a discussion of this will be reserved until later.

The viscous contribution, F_r , which is proportional to $\sigma\Gamma$ and hence the swirl velocity difference $V_i - V^*$, contributes to the cross stiffness only. The physical reason that this force is independent of the whirling frequency is that it depends on a velocity difference which is necessarily independent of any change of reference frame due to the whirl. The mechanism that produces this force is shown Figure 7. The flow enters the offset seal with a higher swirl velocity than exists inside the seal. Less excess momentum enters through the narrow gap on the right than the wider gap to the left. As the flow mixes out, it energizes the fluid inside the gland increasing the static pressure like an ejector pump. The place with the highest pressure will be at the bottom yielding a positive cross force as shown. A simple analysis of this is done by using the following simplified momentum equation

$$\bar{q}(V - V_i) + \frac{lh}{R_s} \frac{\partial P}{\partial \theta} = 0 \quad (31)$$

this expression can be integrated to yield the viscous cross force

$$F_r = \frac{i\pi q^* R_s^2 (V_i - V^*) \hat{r}}{h \delta_1^*} \quad (32)$$

From Equation (26) the relative magnitudes of the ideal and viscous contributions are found. Two limiting cases are possible

$$|\Gamma| = \left| 1 - \frac{V_i}{V^*} \right| \ll |D| = \left| \frac{\delta_1^*}{h} \right| \quad \text{friction is unimportant} \quad (33)$$

$$|\Gamma| = \left| 1 - \frac{V_i}{V^*} \right| \gg |D| = \left| \frac{\delta_1^*}{h} \right| \quad \text{friction is dominant} \quad (34)$$

However, in real hardware it is more common to have $|\Gamma| \cong |D| \cong 0.05$ and hence, both contributions must be accurately modeled.

Figure 8 shows the cross force vs. the non-dimensional whirling frequency, W for an ideal and real flow. Here increasing viscosity means that the swirl change is becoming more negative through viscous action either through higher friction factors or lower rotational speeds (in the direction of inlet swirl). As stated, the cross force vanishes for an inviscid flow when $W=1$. That is, when the gap travels at the swirl velocity. When the presence of viscosity is considered the cross force increases the same at all whirl frequencies.

If the swirl speed decreases through the seal, as is typical, then the frequency at which the force becomes negative shifts to a higher W , as shown.

4. EXPERIMENTAL APPARATUS

The Labyrinth Seal Test Facility (LSTF) was designed and built to measure the dynamic forces in a spinning/whirling labyrinth seal. Figure 9 shows a cross section of the hardware. Air from a compressor enters the first plenum and is turned radially outward through eight 1 and 1/2 inch holes having honeycomb plugs. Next the air turns axially and accelerates through a set of replaceable swirl vanes into the swirl plenum. The air flows through the test seals and discharges to the atmosphere. The spinning/whirling motion of the seal is produced by the nested bearing arrangement. Different whirl amplitudes are obtained by adjusting the inner spindle bearing seat eccentricity. The spin motion (+6700rpm to -6700 rpm) is driven by an in-line flexible coupling driven by an electric motor. The speed of the whirling motion, which can be controlled independently, (+3400 rpm to -3400 rpm) is driven by a V-belt attached to another motor. Four equally spaced, flush mounted, high response, Kulite XCS190 differential pressure transducers were placed on the seal land to measure the time resolved gland pressure oscillations created by the seal whirling motion. The back pressure ports were referenced to the gland average pressure to obtain higher sensitivity. Proximometers were used to precisely measure the whirling motion. Measurements of the swirl angle leaving the second knife were made with a hot wire anemometer. The data acquisition system was triggered and clocked with a chopper wheel attached to the whirl producing spindle. Thirty-two phase locked points were taken for each whirl revolution. Records of 64 revolutions were taken. The pressures were composite phase-locked ensemble averaged to find the forces acting on the rotor for each operating condition. A total of five different seal geometries, shown in Table 1, were tested under various operating conditions. The inlet pressure, swirl vane angle, spin velocity, whirl eccentricity and frequency were varied parametrically. Figure 10 shows a typical output trace from one of the Kulites versus data point number. Note the periodicity of 32 data points per cycle as expected. Spectral analysis of these signals showed that virtually all of the energy of the signal is concentrated at the whirl frequency for cases with no seal rotation [24]. For cases including rotation, a small harmonic component, with amplitude of about 5% of the primary component due to whirl, at the spin frequency was present. This was due to very small deviations from circularity of the seal.

5. COMPARISON OF EXPERIMENTS TO THEORY

A strict comparison of the preceding theory with coupling to the LSFT test results is not possible because of the lack of control over the axial leakage gap, δ_c , the importance of which was shown in Section 2. What can be shown, however, is that for the range of likely values of δ_c , the upstream coupling effects increase the cross forces the required amount to explain the very large deviations between experimental data and the simple, uncoupled theory.

The general character of the comparison can be seen from Figure 11, which shows the nondimensional cross stiffness versus the nondimensional inlet swirl. The trends and comparisons for C_{xx} are the same as for K_{xy} , due to the relationships shown in Section 3. The theoretical lines were calculated using the cavity parameters for Build #3. The volume ratio (upstream to seal cavity) was in that case 3.01, whereas it was 4.64 for Build #2. The amplification factors calculated from the coupled theory (for $\delta_c = 10$ mil) are 3.7 for Build #3 and 2.8 for Build #2.

Looking first at the Build #3 data only, we notice a general grouping about the theoretical line for δ_c between 5 and 10 mil. The design value of this gap was 10 mil. We also see that the points appear in groups, each of which is aligned with a somewhat different δ_c line. These groups in fact correspond to the different swirl vane assemblies, and δ_c can be expected to have remained constant within each of them, but perhaps not with exactly the same value from assembly to assembly.

The data for the two outer groups of points for Build #2 are roughly on a line with a slope lower by 1/1.3 than those for Build #3, in accordance with the noted difference between the volume ratios of both cases. The group for the smaller dimensionless inlet swirl is anomalously high, however. In general, for all builds, the data are indeed bracketed between the limits of the uncoupled ($\delta_c \rightarrow \infty$) theory and the fully coupled ($\delta_c = 0$) models.

As a related test of the theory, equations were derived for multi-cavity seals with upstream coupling [9]. This coupled theory for a 2-gland seal, plus the upstream cavity was compared to some 2-gland static seal data of Benckert and Wachter [5], whose facility had the same general upstream configuration as the LSTF. These researchers also failed to keep a careful control of their face seal, for which no value is reported. As noted before, no theoretical calculation had been able to match the higher than expected cross-forces in these short seals. Using the coupled model, the cross forces obtained in all three 2 gland seals that Benckert tested can be matched by the theory with appropriate choices of the axial sealing gap, ($\delta_c = 0$) (a slightly different one for each build). Not only can the total force be predicted, but the relative contributions from each gland can be matched for the one case for which this was reported. The model predicts that the effects of the upstream coupling die exponentially. After a few glands the upstream influence cannot be seen. The data of Benckert support this conclusion.

Table 2 gives the data of Benckert along with several cases from the model. The cross force as predicted with uniform upstream conditions is given. Finally, the value of the axial gap that matches Benckert's data is given for each case. These values are reasonable and show that the strong upstream coupling is the most likely cause for the high cross forces generated in the first gland of a seal.

Figure 12 shows a typical plot of the cross force vs. whirl frequency for five different pressure ratios from Build #4. There is no rotation and the nominal inlet swirl angle is 8.6 degrees. The general frequency dependent behavior of the experimental data is well predicted by the analytical model. In particular, the cross force is a linear function of the whirl speed and the frequency at which the force changes sign matches the theoretically predicted value within

experimental uncertainty. Of course the absolute force levels are much higher as predicted by the coupled theory. Figure 13 shows the cross force vs. whirl frequency for five different spin rates for the same build. It can clearly be seen that the data at different spin rates fall on parallel lines. Similar results were found for all builds at all flow conditions. The narrow implication of this is that changes in rotational speed do not affect the damping. More generally, these data strongly support the general validity of the cross force decomposition into ideal and viscous contributions as presented above.

The method presented above for predicting the dynamic coefficients from inviscid static values can be readily extended to cases with "viscosity" if the frictional component is isolated properly. Probably the best method for removing this frictional "contamination" is to handle it directly in the experiment. If the inlet and exit swirl velocities are measured then for every value of the inlet swirl the seal spin speed should be adjusted to maintain a constant swirl difference, $V_i - V^*$. Hence, the additive frictional component is fixed. For $V_i = V^*$, the viscous component is totally eliminated. For typical designs the spin speed needs to be maintained at about 125% of the inlet swirl velocity to keep $\Gamma = 0$. If this procedure is not followed the measurements of a statically offset seal can still be used to obtain damping data. If static data is taken with no rotation, a correlation of the cross stiffness coefficient, K_{xy}^* , versus swirl parameter, σ , can be obtained. The problem is that as the inlet swirl velocity is increased the total cross force increases due to a higher inlet swirl (inviscid contribution) as well as the frictionally induced change in swirl. The change in the ideal component with inlet swirl, which is equal to the direct damping must be separated. One procedure is to use the static correlation to calculate a total force, $F_T(\Omega_d R_s)$, at an inlet swirl velocity corresponding to a whirl frequency Ω_d . The viscous force, found from theory or correlation, is subtracted from the total force to yield the ideal component. The damping is the rate of change of this force with frequency.

$$C_{xx} = \frac{F_T(\Omega_d R_s) - F_V(\Omega_d R_s)}{\Omega_d} = \frac{F_I(\Omega_d R_s)}{\Omega_d} \quad (35)$$

The values of the direct damping, C_{xx} , calculated from the static measurement correlations employing this method agree with the values that were directly measured in the dynamic mode to within 13%, 8% and 15% for builds 2,3 and 4 respectively as shown in Table 3. This demonstrates that it is possible to predict the dynamic coefficients with the use of static measurements only. Another method for extracting the dynamic coefficients from static data, based on extrapolation, is presented by Millsaps and Martinez-Sanchez [26].

6. CONCLUSIONS

A new theory was developed that contains the effect of flow coupling. It was shown that this theory is capable of predicting the larger than expected forces found experimentally.

This finding has several important implications for design and analysis of short labyrinth seals, and, by extension, probably for other seal types as well. Data on cross forces from such seals should be

supplemented by a description of the upstream (and also the downstream) configuration of the test device, unless it can be ascertained by auxiliary tests that no coupling exists. As an example of the latter situation, it was verified that the rotordynamic force data were insensitive to the downstream configuration. This was found by blocking parts of the exhaust holes from the downstream chamber. The remaining holes were large enough to equilibrate this chamber with the atmosphere, hence making coupling negligible.

Calculation of seal rotordynamic coefficients, either for design or for rotordynamic diagnostic purposes, should always account for these possible coupling to the external flowfield. Ignoring them may make other refinements, such as more precise 2 or 3-D cavity flow modeling or CFD calculations irrelevant by comparison. Including the upstream and downstream coupling is relatively straightforward for simple geometries, such as the LSTF rig, but no theory currently exists that can be used to predict the non-uniformities ahead of, for example, the seal on a turbine tip shroud, where the tip area interacts strongly with the main turbine through flow. Development of such a theory would seem important. Similar considerations should apply for other seal environments.

In future designs of rotordynamic testing devices, consideration should be given to either minimizing the coupling mechanisms or matching the expected coupling levels that may occur in a real turbomachine. In any case measurements of the flow field upstream and downstream should be done to assess the degree of non-uniformity induced from the offset seal.

The following conclusions on the nature of rotordynamic damping have been drawn from consideration of the analytical model and the supporting experimental data.

1. The total cross force acting on a labyrinth seal at a given whirl frequency can be decomposed into "ideal" and "viscous" components.
2. The ideal component, which is due to an inviscid swirling flow, is a unique function of the inlet swirl relative to the gap variation phase speed. This force component vanishes when the velocity of the traveling gap is equal to the swirl velocity inside the gland. This component is solely responsible for damping.
3. The viscous component does not create nor alter the direct damping. It adds to (if the swirl velocity decreases in the gland) or subtracts from (if the swirl increases) the cross stiffness only.
4. The direct damping can be calculated from measurements of cross stiffness. The importance of this is that difficult and expensive dynamic measurements are not necessary in order to obtain damping coefficients.

REFERENCES

1. Den Hartog, J. P., 1956, Mechanical Vibrations, 4th Edition, McGraw Hill, pp. 319-321.

2. Alford, J. S., 1965, "Protecting Turbomachinery form Self-Excited Rotor Whirl", Journal of Engineering for Power, October, pp. 333-344.
3. Thomas, H. J., 1958, "Instabile Eigenschwing von Turbinelauefern Angefacht durch die Spaltstroemung in Stopfubuchseen und Bechauchflug (Unstable Natural Vibrations of Turbine Rotors Induced by the Clearance Flows in Glands and Blading)", Bull. de L.A.I.M. 71 No. 11-12, pp. 1039-1063.
4. Kostyuk, A. G., 1972, "A Theoretical Analysis of the Aerodynamic Forces in the Labyrinth Glands of Turbomachines, Teploenergetica, Vol. 19, No. 11, pp. 29-33.
5. Iwatsubo, T., 1980, "Evaluation of Instability Forces in Labyrinth seals in Turbines or Compressors", NASA CP-2133, pp. 139-169.
6. Gans, B. E., 1983, Prediction of Aeroelastic Forces in a Labyrinth Type Seal and its Impact on Turbomachinery Stability, Eng. Thesis, Department of Mechanical Engineering, M.I.T.
7. Kurahashi, Y., Inoue, T., 1980, "Spring and Damping Coefficients of Labyrinth Seals", Proceedings of the Institute of Mechanical Engineers.
8. Fujikawa, T., Kameoka, T., Abe, T., 1984, "A Theoretical Approach to Labyrinth Seal Forces.", NASA CP-2338, pp. 28-30.
9. Scharrer, J. K., Childs, D. W., 1989, "Theory vs. Experiment for the Rotordynamic Coefficients of Labyrinth Gas Seals", Parts 1&2, ASME Journal of Vibration, Acoustics, Stress and Reliability in Design, Vol. 110, No. 3, pp. 270-287.
10. Martinez-Sanchez, M., Lee, O. W. K., Czajkowski, E., 1984, "Prediction of Force Coefficients in Labyrinth Seals", NASA CP-2338, pp. 235-256.
11. Jenny, R. J., Wyssmann, H. P., Pham, T. C., 1984, "Prediction of Stiffness and Dynamic Coefficients for Centifical Compressor Labyrinth Seals", ASME 84-GT-86, 29th International Gas Turbine Conference, June 4-7, Amsterdam, The Netherlands.
12. Nordman, R., Weiser, P., 1990, "Evaluation of Rotordynamic Coefficients of Look-Through Labyrinths by Means of a Three Volume Bulk Flow Model", Sixth Workshop on Rotordynamic Instability. Texas A&M Univ., May 21-23, pp. 141-157.
13. Benckert, H., 1980, Stromungsbedinte Federkennwerte in Labyrinthdichtungen, Doctoral Dissertation, University of Stuttgart.
14. Benckert, H., Wachter, J., 1978, "Querkraefte aus Spaltdichtungen - Eine Mogliche Ursache fur die Laufunruhe von Turbomachinen, Atomkernenergie, Bd. 32, Lfg. 4, pp. 239-246.

15. Benckert, H., Wachter, J., "Flow Induced Spring Coefficients of Labyrinth Seals for Applications in Rotordynamics", NASA CP-2133, pp. 189-212.
16. Brown, R. D., Leong, Y. M. M. S., 1982, "Circumferential Pressure Distributions in a Model Labyrinth Seal", NASA CP-2133, pp. 222-232.
17. Thielele, G., Stetter, H., 1990, "Experimental Investigation of Exciting Forces in Labyrinth Seals", Sixth Workshop on Rotordynamic Instability. Texas A&M University, May 21-23, pp. 141-157.
18. Kanki, H., Morii, S., 1985, "Destabilizing Forces in Labyrinth Seals", NASA CP-2409, pp. 205-223.
19. Hisa, S., Sakakida, H., Asatu, S. , 1986, "Steam Excited Vibrations in Rotor-Bearing Systems", Proceedings of the International Conference on Rotordynamics", Sept. 14-17, Tokyo, pp. 635-641.
20. Wright, D. V., 1978, "Air Model Tests of Labyrinth Seal Forces on a Whirling Rotor", Journal of Engineering for Power, Series A , Vol. 100, No. 14, October, pp. 533-543.
21. Kanemitsu, Y., Ohsawa, M., 1986, "Experimental Study on Flow Induced Forces of Labyrinth Seals", Proceedings of the IFTOMM Conference on Flow induced Force in Rotating Machinery, Sept. 18-19, Kobe University, Japan, pp. 106-112.
22. Scharrer, J. K., 1987, A Comparison of Experimental and Theoretical Results for Labyrinth Gas Seals, Ph.D. Dissertation, Mechanical Engineering Department, Texas A&M University.
23. Millsaps, K. T., Martinez-Sanchez, M., 1990, "Static and Dynamic Pressure Distributions in a Short Labyrinth Seal", NASA CP-2543., pp. 129-140.
24. Millsaps, K. T., 1992, The Impact of Unsteady Swirling Flow in a Single Gland Labyrinth Seal on Rotordynamic Stability: Theory and Experiment, Ph.D. Dissertation, Department of Aeronautics and Astronautics, M.I.T.
25. Varnes, G., 1960, "A Fluid Mechanics Approach to the Labyrinth Seal Leakage Problem", Journal of Basic Engineering, Transactions of the ASME, Series D, Volume 82, No. 2, pp. 265-275.
26. Millsaps, K. T., Martinez-Sanchez, M., 1993, "Dynamic Forces From Single Gland Labyrinth Seals: Part I - Ideal and Viscous Decomposition, International Gas Turbine Conference, Cincinnati, OH.
27. Millsaps, K. T., Martinez-Sanchez, M., 1993, "Dynamic Forces From Single Gland Labyrinth Seals: Part II - Upstream Coupling, International Gas Turbine Conference, Cincinnati, OH.

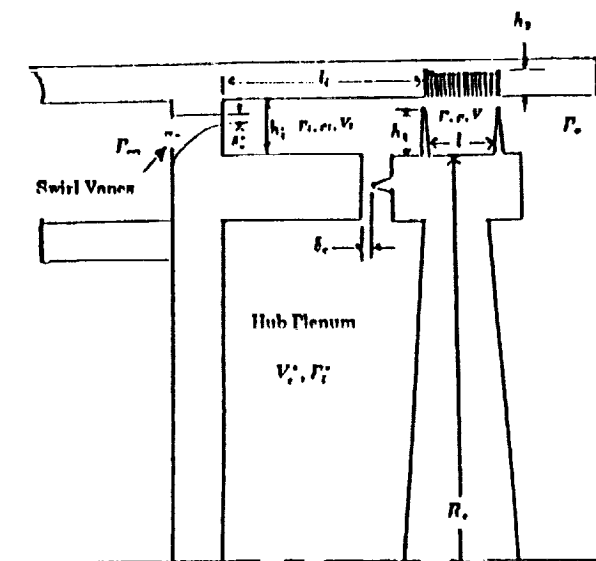


Figure 1. Schematic of Labyrinth Seal Test Facility test section showing upstream swirl cavity and the flows into and out of the center hub plenum.

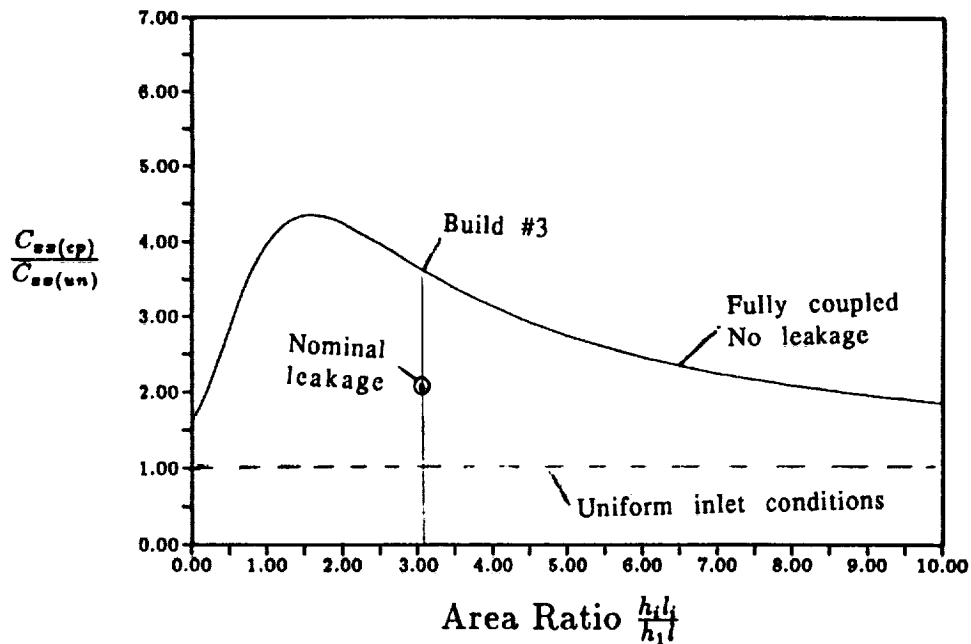


Figure 2. Ratio of rotordynamic damping with upstream coupling to that with no coupling versus swirl cavity to seal gland area ratio.

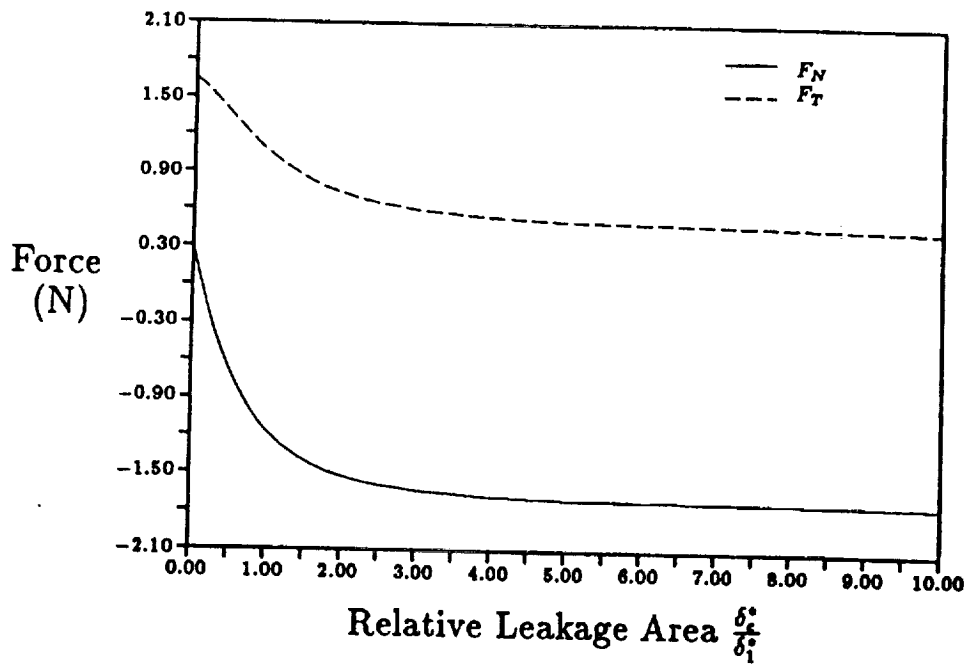


Figure 3. Predicted direct and cross force at $\Omega=0$ for the coupled model versus the relative axial clearance. The geometry is the same as for build #3. $\pi_s=1.4$, $\alpha_v=15$ degrees, $\epsilon_1=0.1407$ and $\omega=0$.

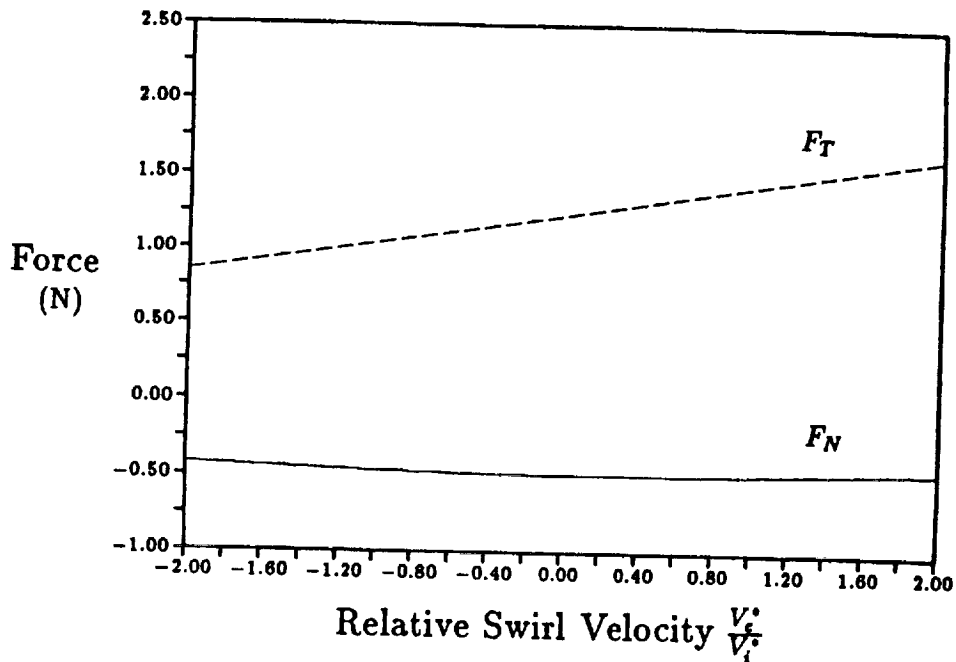


Figure 4. Direct and cross force predicted by the coupled model versus the center cavity swirl velocity. These are for the same conditions as Figure 3.

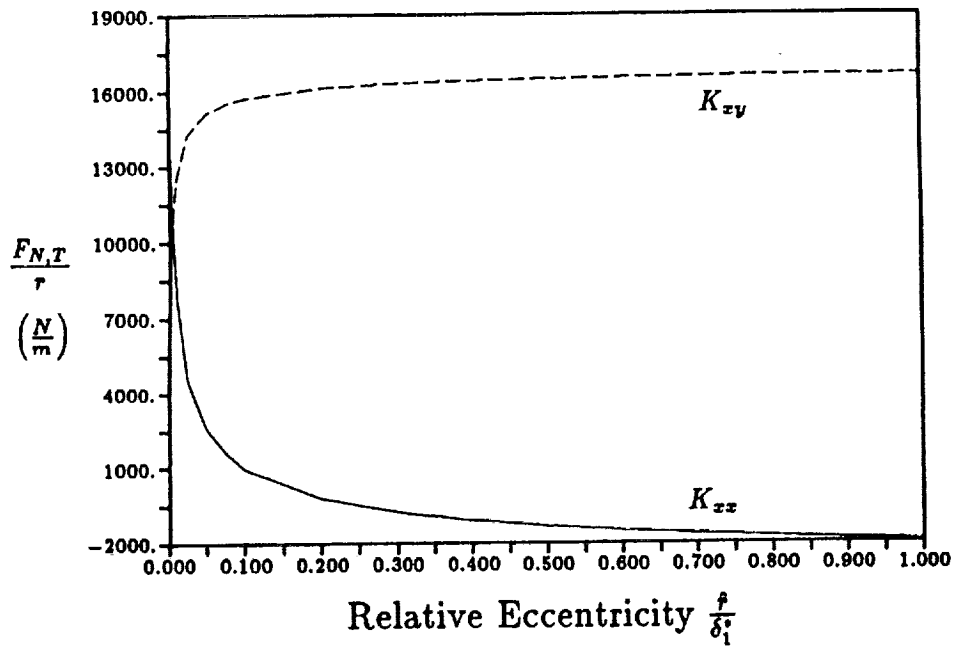


Figure 5. Effect of relative whirl amplitude on the direct and cross stiffness as predicted by the coupled model with hub leakage. Build #3 geometry and $\delta_c / \delta_1^* = 0.19$.

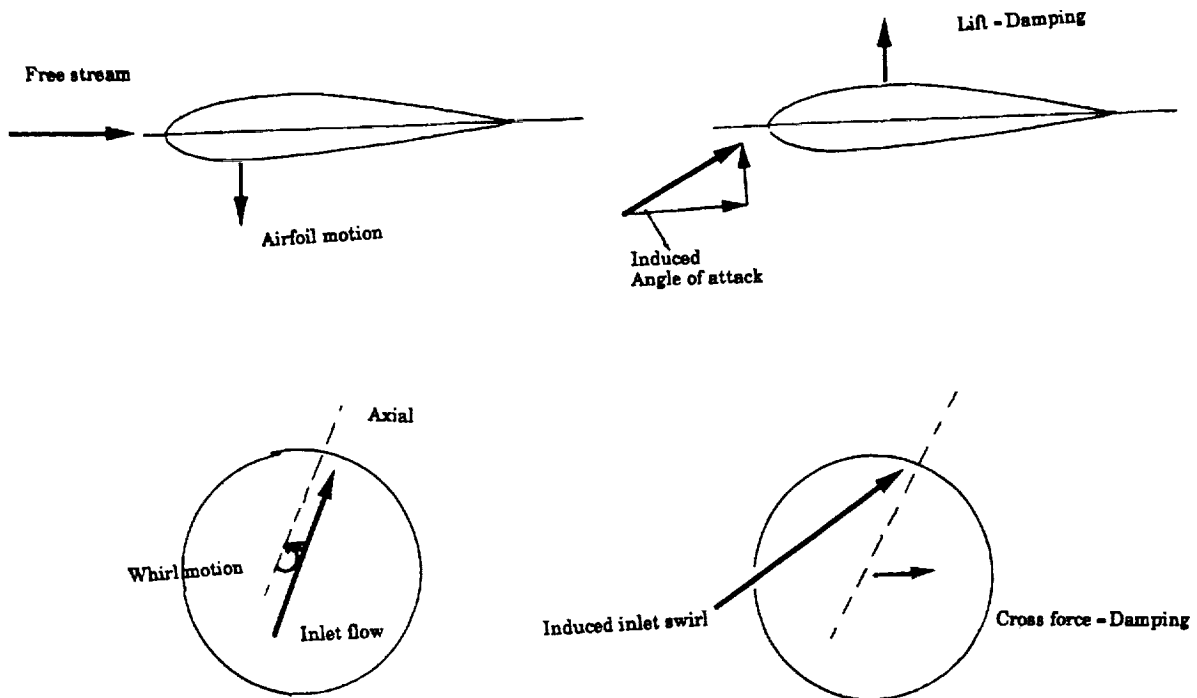


Figure 6. Analogy between quasi-static damping of a translational airfoil generating an induced angle of attack and a whirling seal inducing a inlet swirl component.

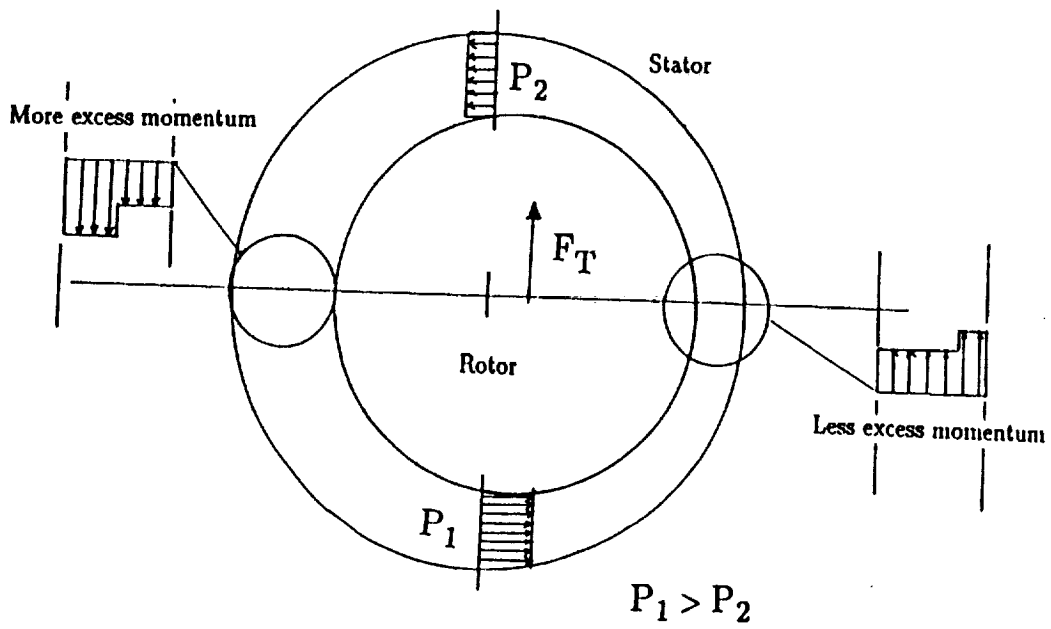


Figure 7. Physical origin of the viscous force. This force is due to a velocity difference and hence is independent of the whirl frequency. Therefore, it does not contribute to the damping.

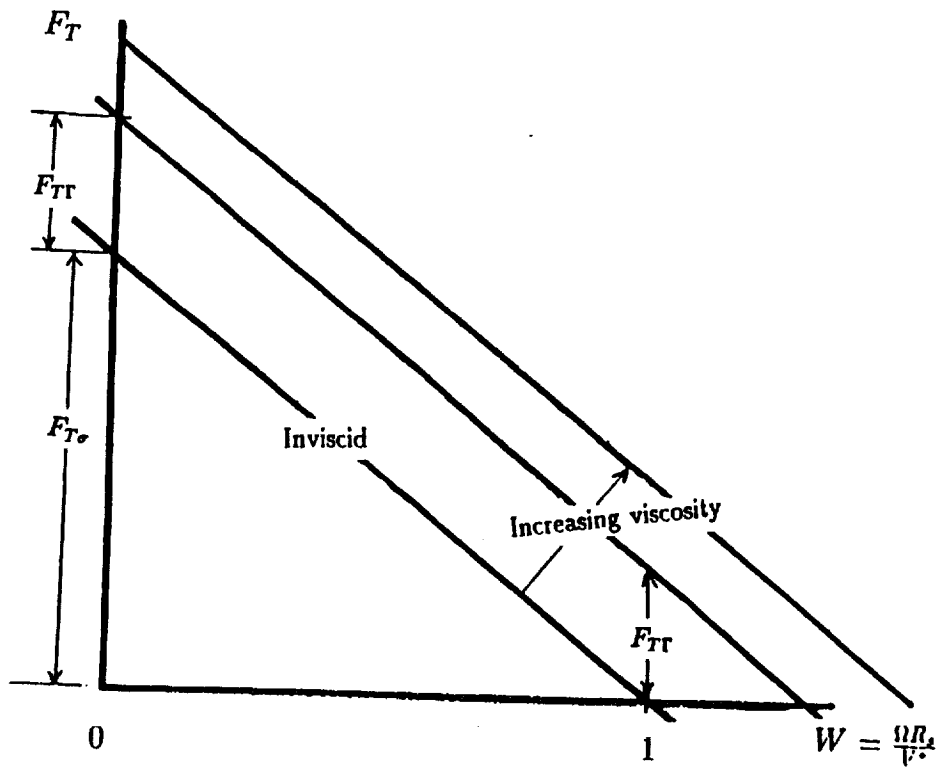


Figure 8. General frequency dependent behavior of the cross force, showing both the ideal and viscous contributions.

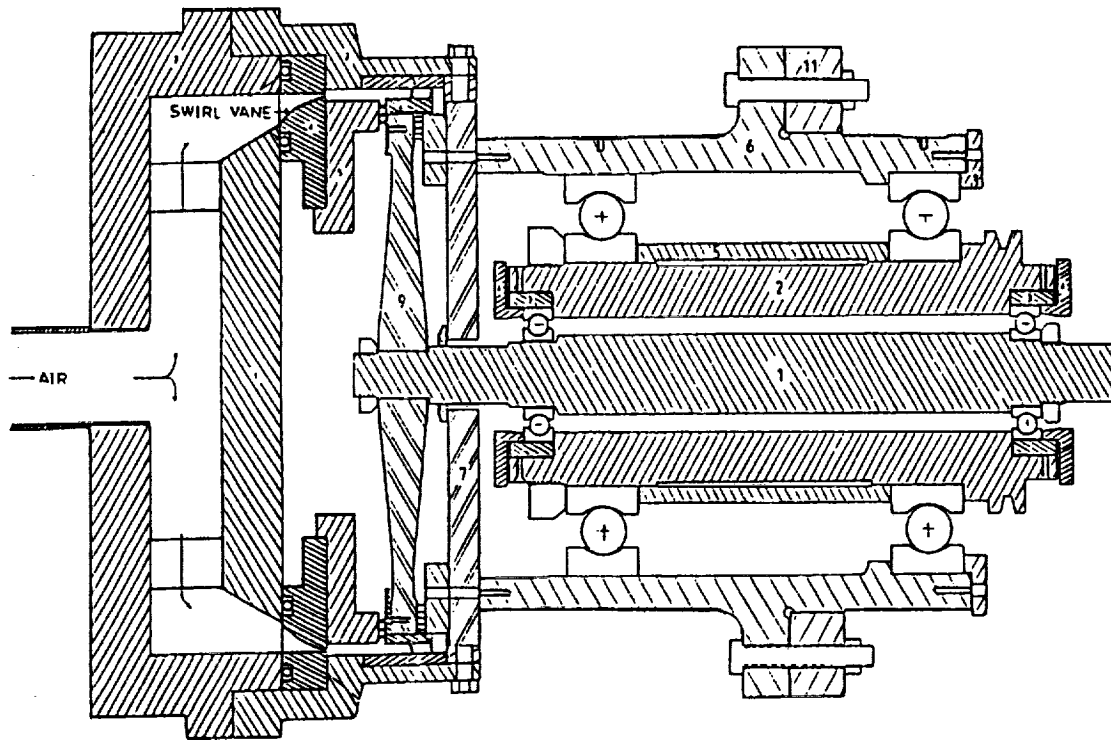


Figure 9. Cross section of the LSTF test section and nested spindle whirl/spin producing rotating machinery.

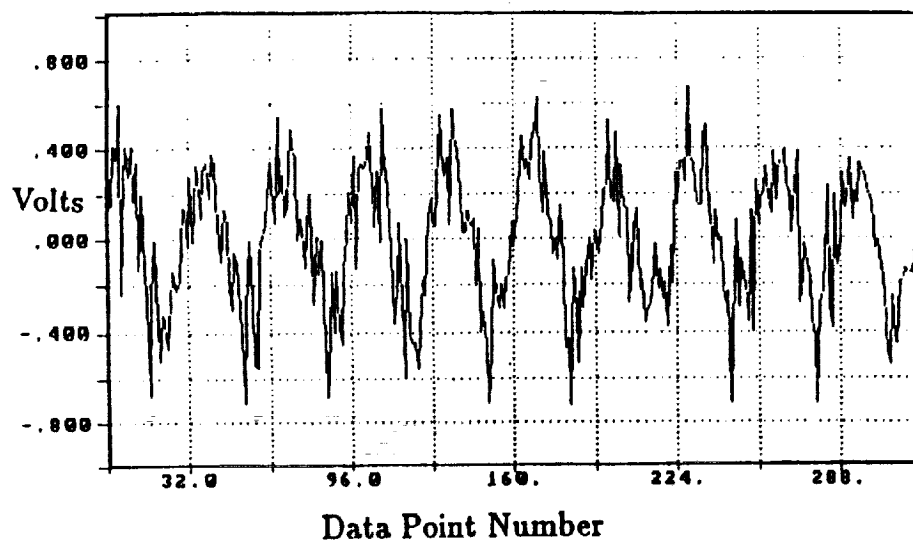


Figure 10. Typical output trace from one of the flush mount pressure transducers. There are 32 data points per whirl revolution.

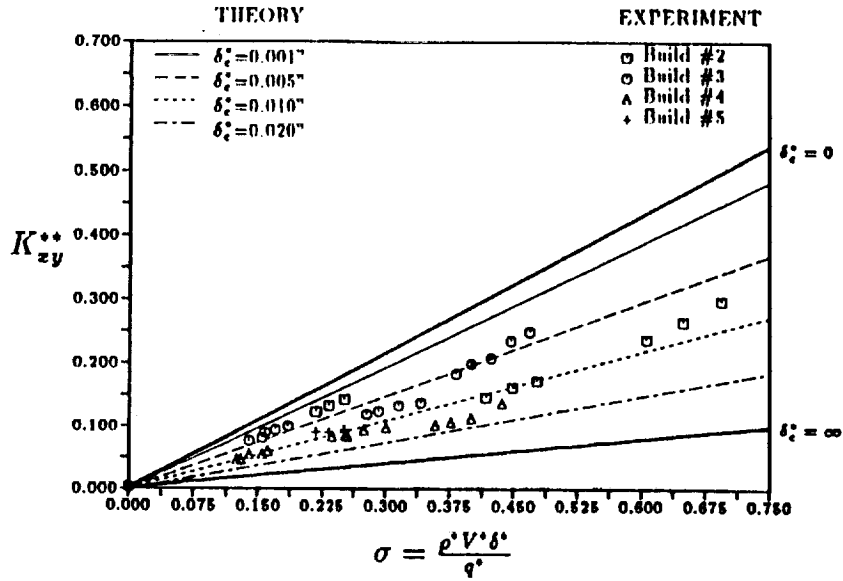


Figure 11. Nondimensional cross stiffness, K_{xy} , versus the swirl parameter, σ , for the experimental data and theory, with the axial gap used as a parameter. All experimental values fall between the theoretical predictions with $0.004'' (0.0001m) < \delta_c < 0.017'' (0.0004m)$. The top thick line is the fully coupled case (i.e. no center leakage) and the bottom on is for uniform inlet conditions (i.e. no coupling). Calculations are for build #3 geometry.

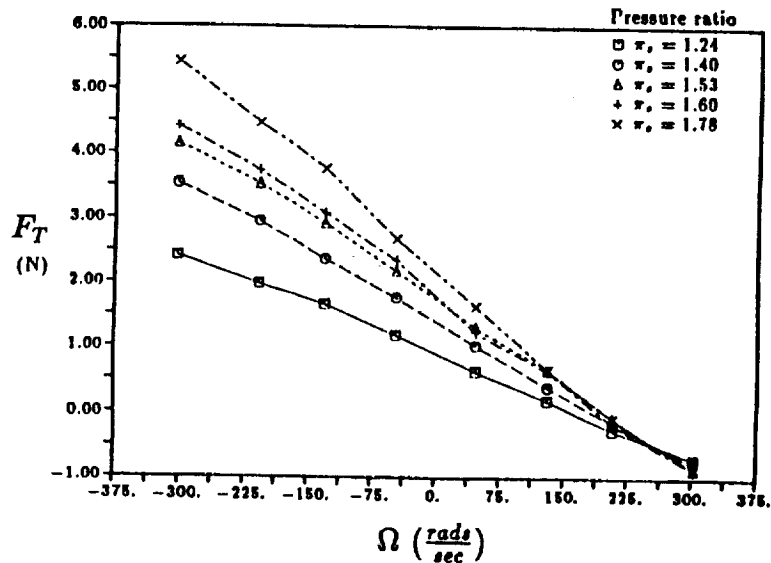


Figure 12. Experimentally obtained cross force versus whirl frequency for five different pressure ratios. These data are from build#4 with 8.6 degrees of inlet swirl and no shaft rotation.

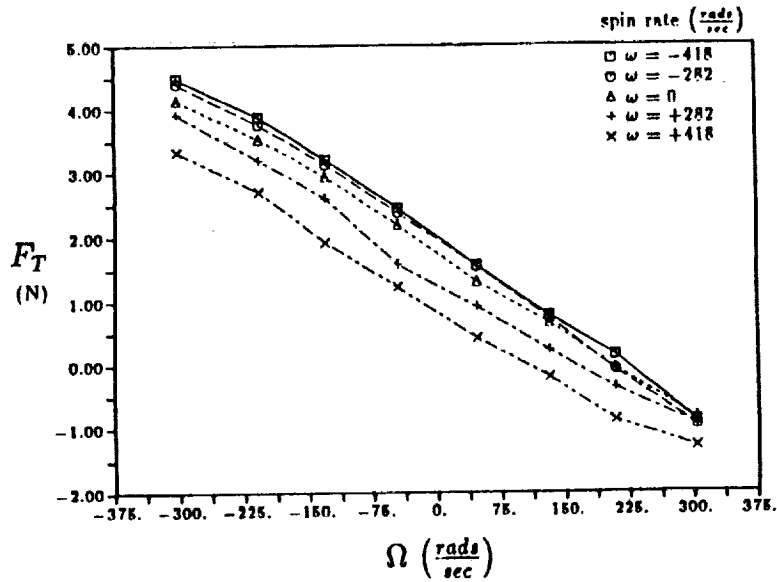


Figure 13. Experimentally obtained cross force versus whirl frequency for five different seal spin rates. These data are from build#4 with 8.6 degrees of inlet swirl and the pressure ratio is 1.47.

Table 1. Geometry for the five seal builds.

BUILD	SEAL DIMENSIONS (rotor)						LAND DIMENSIONS (stator)				
	Material	R_s	l	h_1	d	α_s	Material	ϕ_s	h_2	l_2	δ_1^*
#1	4140	15.166	1.016	0.508	0	20°	1117	15.240	0	0	0.0737
	steel	5.971	0.400	0.200	0		steel	6.000	0	0	0.029
#2	4140	15.166	1.016	0.508	0	20°	1117	15.246	0	0	0.0787
	steel	5.971	0.400	0.200	0		steel	6.002	0	0	0.031
#3	304 SS	15.177	1.727	0.508	0.043	17°	1117	15.246	0	0	0.0686
	steel	5.975	0.680	0.200	0.017		steel	6.002	0	0	0.027
#4	304 SS	15.177	1.727	0.508	0.043	17°	304 SS	15.246	0.483	1.905	0.0686
	steel	5.975	0.680	0.200	0.017		Hastelloy X	6.002	0.190	0.750	0.027
#5	4140	15.166	1.016	0.508	0	17°	304 SS	15.246	0.483	1.905	0.787
	steel	5.970	0.400	0.200	0		Hastelloy X	6.002	0.190	0.750	0.031

Table 2. Comparison of the static data of and Wachter to the coupled model. The first column shows the experimental value. The second column gives the value predicted with full coupling. The third gives predictions for constant upstream conditions (i.e. no coupling). The last column gives the value of the axial sealing gap needed for the model to match the experimentally obtained value.

CONFIG.	$F_T(meas.)$	$F_T(\delta_c^* = 0)$	$F_T(\delta_c^* = \infty)$	Matched δ_c^*
1	10.21(N)	16.28(N)	4.99(N)	0.008"
2	8.28(N)	16.15(N)	4.25(N)	0.011"
3	11.91(N)	15.51(N)	4.09(N)	0.010"

Table 3. The first column gives the cross stiffness correlation coefficient obtained from static measurements. The next two columns give the total, and frictional force, respectively calculated at a whirl speed of 300 (rads/sec). The last two columns give the calculated and measured direct damping coefficients.

BUILD#	$\frac{\partial K_{xx}^{**}}{\partial \sigma}$	$\frac{F_T(\Omega_d)}{f}$	$\frac{F_{TF}(\Omega_d)}{f}$	C_{xx}^{**}	From Static Correlation $C_{xx} \left(\frac{Ns}{m} \right)$	Measured Directly $C_{xx} \left(\frac{Ns}{m} \right)$
2	0.372	7763	953	0.289	22.70	19.95
3	0.416	27821	3162	0.371	82.19	75.80
4	0.283	20001	3162	0.247	56.13	48.54
5	0.338	7053	953	0.231	20.33	15.81

